Check for updates

LiCl modified MOFs-derived porous carbon hollow spheres for efficient solar-driven atmospheric water harvesting

Jiake Jin,[†ab] Simiao Guo,[†ab] Yue Hu,[ab] Yefeng Yang, [ID][bc] Pingwei Ye*[d] and Xinsheng Peng [ID] *[ab]

Developing adsorbents with excellent photothermal and water uptake properties for solar-driven sorption-based atmospheric water harvesting (SAWH) is full of challenging, which requires a balance between the adsorption capacity, hydrophilicity, and photothermal performance of adsorbent. In this work, a LiCl modfiied porous carbon hollow microspheres (CHM@LiCl) adsorbent with high adsorption capacity (2.07 g g^{-1}) at 100% RH and enhanced low moisture adsorption performance was synthesized by loading LiCl hydrophilic adsorption sites into MOFs-derived hollow porous carbon. LiCl, as the main adsorption site, enhances the hydrophilicity of the CHM@LiCl adsorbent, and its water uptake capacity at 20% RH, 40% RH, 60% RH, and 80% RH are 0.25, 0.39, 0.60 and 1.04 g g^{-1}, respectively. In addition, the hiearchical porous structure of the hollow carbon with mciroporous shell effectively suppresses the salt leakage during water adsorption. The sorbent exhibits stable performance for cycling water adsorption-release, indicating its long-term reliability. The excellent photothermal performance of CHM@LiCl adsorbent can quickly heat up to 67 °C under one sun irradiation, and completely desorb the adsorbed water within 30 minutes. The outdoor water harvesting experiment shows that the CHM@LiCl adsorbent holds great potential for practical solar-driven SAWH with a water collection capacity of 3.3 L$_{water}$ kg$_{sorbent}$$^{-1}$ day under RH 60%.

Introduction

As one of the most critical global issues, water scarcity requires ongoing attention due to the uneven distribution of freshwater resources worldwide.[1] Considering the quality of surface water, recent studies have revealed a concerning statistic: approximately 55% of the global population, or 3.8 billion people, now face a scarcity of clean water for at least one month each year.[2] This growing issue highlights the urgent need for effective water harvesting strategies and the protection of freshwater resources. Fortunately, apart from traditional freshwater sources like groundwater, rivers, and lakes, the atmosphere contains ample and sustainable water-around 12 900 cubic kilometers, which holds significant potential to alleviate global water scarcity.[3]

Atmospheric water exists in both liquid and gaseous forms. Liquid water encompasses clouds and fog. The former can be harvested through cloud seeding, a technique that aids in addressing immediate agricultural needs while also contributing to the sustainable management of water resources over the long term.[4] Fog, though more common, is typically found in coastal arid regions or around cooling towers in thermal power plants. It can primarily be collected using mesh or wire fog collectors.[5,6] Gaseous water, or water vapor, is present everywhere in the atmosphere and can be harvested through active or passive condensation into dew drops, or by sorbents that adsorb and release moisture.[7,8] In contrast to the energy-intensive condensation process and the geographically limited fog collection, sorption-based atmospheric water harvesting (SAWH) technology holds greater potential for widespread application, particularly in regions with low relative humidity (RH).[9] The SAWH technology works as follows: during the night with low temperature and high RH, it is exposed to the atmosphere to absorb water molecules from the air and then store the water. During the daytime with high temperature and intense solar illumination, it is enclosed in the room, absorbs solar energy to convert the water absorbed at night from the liquid phase back to the gaseous phase. Meanwhile, the gaseous water molecules are liquefied on condensation plate at relatively low-temperature to form clean water, which is then collected.

aState Key Laboratory of Silicon Materials, School of Materials Science and Engineering, Zhejiang University, Hangzhou 310027, People's Republic of China. E-mail: pengxinsheng@zju.edu.cn

bWenzhou Key Laboratory of Novel Optoelectronic and Nanomaterials, Institute of Wenzhou, Zhejiang University, Wenzhou 325006, P. R. China

cSchool of Materials Science and Engineering, Zhejiang Sci-Tech University, Hangzhou 310018, China

dState Key Laboratory of Chemistry for NBC Hazards Protection, Beijing, 102205, P. R. China. E-mail: yepw2001@163.com

† The authors' contributions are equal.

Sorbents used in SAWH can be broadly categorized into metal–organic frameworks (MOFs),[10,11] salt-based composite sorbents,[12–15] polymer networks,[16–18] and porous carbon materials.[19,20] Among these, MOFs have attracted significant attention due to their tunable structure and functionality, making them the focus of extensive research in the field of water adsorption. However, achieving a balance between the adsorption capacity and hydrophilicity of MOFs through structural design remains a challenge, particularly when aiming to enhance their water adsorption performance in low-humidity environments. Salt-based composite sorbents are typically created by integrating deliquescent salts into porous matrices, such as MOFs or polymer networks, which exhibit high hydrophilicity and adsorption capacity. The deliquescent salt acts as the primary adsorption site, and its content directly influences the final water adsorption performance. An excessive salt loading, however, can lead to salt leakage issues during practical applications, ultimately reducing the efficiency of the sorbents. While porous carbon materials possess abundant porosity, the intrinsic hydrophobicity significantly limits its ability to capture water in low-humidity conditions. Therefore, further optimization is required to enhance their SAWH performance. This includes improving the hydrophilicity, increasing water adsorption capacity in low-humidity environments, and addressing potential issues such as salt leakage in composite sorbents.

During the desorption phase, heating is typically employed to facilitate the release of water molecules from the sorbent. Solar energy, as a clean and renewable resource, has been increasingly utilized to drive the desorption and regeneration of sorbents due to its simple operation and environmental friendliness.[21] Solar-driven SWAH systems can operate spontaneously without requiring additional energy inputs. However, this necessitates that the sorbent has excellent photothermal conversion capabilities to achieve localized heating of the water molecules.[22] While incorporating photothermal components through post-modification may not only hinder the transport of water molecules to the adsorption sites but also reduce the overall adsorption capacity.[7] A promising approach to address this challenge involves the incorporation of photothermal ligands into the framework of MOFs through structural modification.[23] However, this method requires careful control of reaction conditions, and the interaction mechanisms between the photothermal and hydrophilic components remain underexplored.[23]

MOFs derived porous carbon materials have already been applied in the field of SAWH due to their abundant porosity and polar adsorption sites, which facilitate the capture of water molecules.[24] Additionally, these materials exhibit exceptional photothermal properties, enabling them to adsorb significant amounts of solar radiation and convert it into heat, thereby accelerating the release of water molecules.[24] Nonetheless, one of the key challenges currently is improving the adsorption performance of porous carbon materials in low-humidity environments. This requires not only optimizing the materials' hydrophilicity but also enhancing their photothermal efficiency, especially under varying environmental conditions.

Therefore, in this study, a hollow MOFs-derived porous carbon hollow sphere (CHM) sorbent modified with hygroscopic salt (LiCl) (CHM@LiCl) was synthesized for efficient solar-driven SAWH. The hollow MIL-101(Cr) structure was first prepared through an etching strategy, followed by pyrolysis process and solution impregnation method to introduce LiCl into the resulted CHM. The CHM@LiCl-3 with 13.4 wt% LiCl exhibited a high adsorption capacity over a wide range of relative humidity (20–100% RH), excellent light absorption (~90%), and impressive photothermal heating ability (67 °C under one Sun irradiation). LiCl, serving as the primary adsorption site, significantly enhanced the hydrophilicity of the MOFs-derived hollow porous carbon spheres, thereby promoting water adsorption under low-humidity conditions. Additionally, the microporous shell of the hollow carbon spheres ensures the spatial confinement of the salt in hollow cavities and effectively mitigated the issue of salt leakage during the water adsorption process. Furthermore, CHM@LiCl-3 demonstrated the ability to desorb 100% of the adsorbed water within 10 minutes and exhibited excellent cycling stability, making it a promising candidate for sustainable water harvesting.

Results and discussion

Fabrication and characterization of the sorbents

The preparation process of the CHM@LiCl sorbent is illustrated in Fig. 1a. MIL-101(Cr) was synthesized via a hydrothermal method, and then etched by acetic acid to form hollow MIL-101(Cr) (HM). Subsequently, the porous carbon hollow spheres (CHM) were obtained through a pyrolysis process. Finally, the CHM was modified with LiCl through impregnation process to produce CHM@LiCl sorbents with varied LiCl loading amounts (Table S1). Fig. 1b is a schematic illustration of CHM@LiCl sorbents for solar-driven SAWH. At night, the adsorbent captures water molecules and stores into the hollow cavities. During the day, water was released via photothermal conversion process by sunlight.

As shown in Fig. 2a, MIL-101(Cr) exhibits an octahedral structure, and its characteristic peaks (Fig. 2g and S1a) are consistent with the reported literature, indicating the successful synthesis of MIL-101.[25] The characteristic diffraction peaks occurring at 2θ of 5.13°, 5.85°, 8.5°, 9.1° and 10.4° correspond to the Miller index of (511), (822), (753), (1022) and (880) (Fig. S1a). The peak at 1685 cm^{-1} in FTIR spectrum (Fig. 2h) is corresponds to the C=O peak of 1,4-BDC linker. Due to the interaction between Cr and the carboxylate groups, the C=O peak shifts to 1622 cm^{-1} (Fig. 2h). The symmetric stretching vibration peak associated with the –COO group shifts from 1422 cm^{-1} to a lower wavenumber (1401 cm^{-1}). A new peak around 590 cm^{-1} is corresponding to Cr–O vibrations, indicating the successful synthesis of MIL-101(Cr).[25] The peak at 1510 cm^{-1} corresponds to the C=C stretching vibration on the aromatic ring.[26]

Subsequently, MIL-101(Cr) was etched with acetic acid to form HM. The formation of hollow MOFs is attributed to the presence of more defects inside MOFs, which results in higher surface energy compared to the outer layer. The inhomogeneity
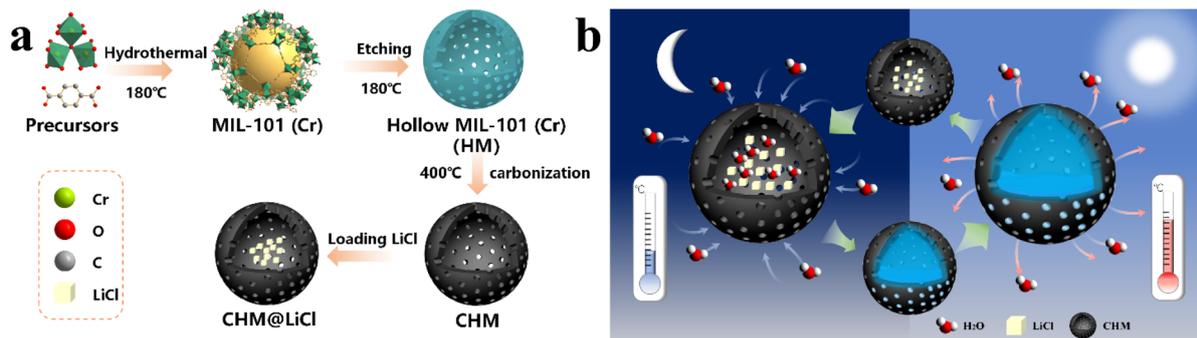
Fig. 1 (a) Schematic illustration of the fabrication process of CHM@LiCl sorbents; (b) schematic illustration of CHM@LiCl sorbents for solar-driven atmospheric water harvesting.

inside MOFs stems from three stages during their synthesis.[27] In the first stage, the solution contains the highest concentration of solutes, leading to the vigorous formation of a large number of high-surface-energy crystal nucleus. In the second stage, to reduce the surface energy in the system, the nuclei undergo rapid agglomeration to form seed crystals, while also introducing numerous defects. The third stage involves increasingly gentle growth on the outside of the seed crystals.

When subjected to etching with acetic acid solution, the inner layers of the MIL-101(Cr) are preferentially dissolved due to their higher reactivity, leading to the creation of a hollow core structure,[28] as depicted in Fig. 2b and c. The average size of HM

ranges from 60 to 150 nm (Fig. S11), and the surface becomes rougher. The characteristic peaks (Fig. 2g and S1a) of HM are similar to those of MIL-101(Cr), but with a slight decrease in peak intensity, which is due to structural defects induced by the etching process.[29] The absorption peaks in the FTIR spectrum (Fig. 2h) of HM do not show significant changes, suggesting that the etching process does not obviously damage the structure of MIL-101(Cr). After carbonization of HM, CHM exhibits more angular features compared to HM (Fig. 2d). It is speculated that this may be related to the decarboxylation and decomposition of the ligand molecule 1,4-BDC and the change in the coordination mode of Cr during the pyrolysis process. The XRD
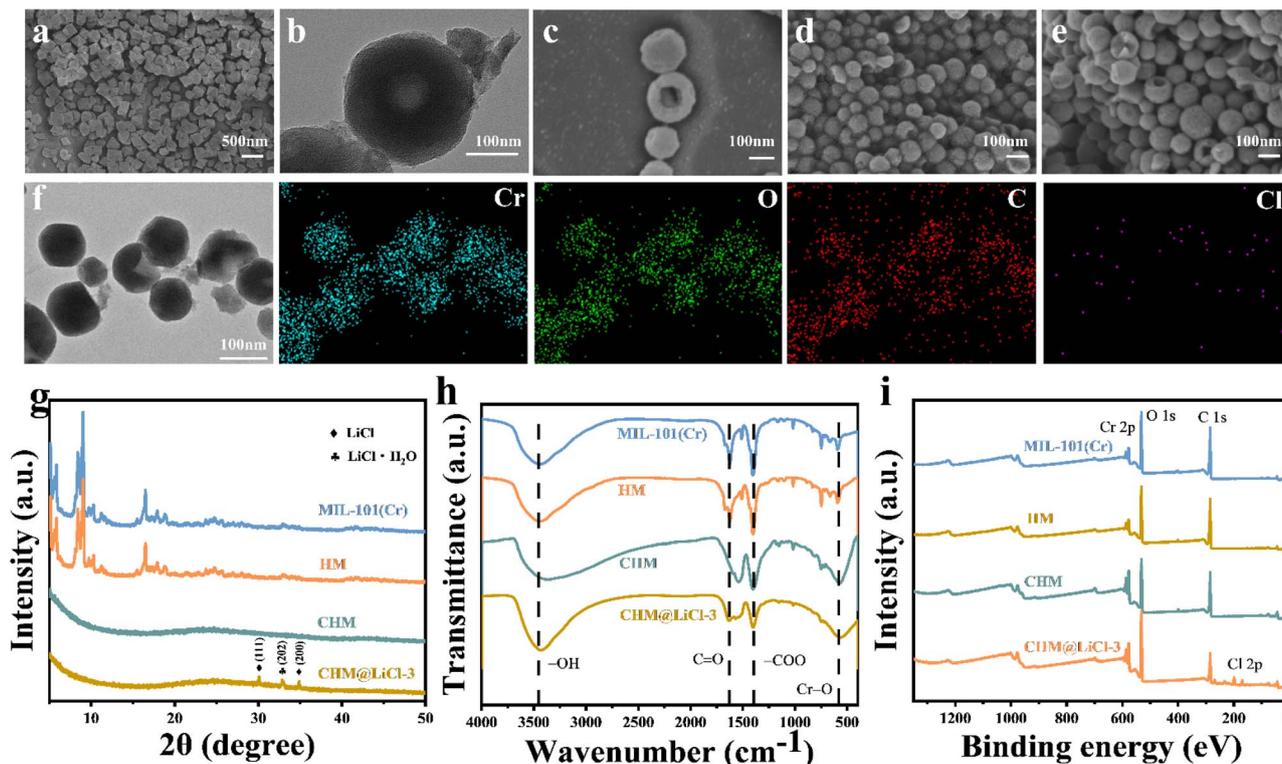

Fig. 2 (a) SEM image of MIL-101(Cr). (b)TEM image and (c) SEM image of HM. SEM images of (d) CHM and (e) CHM@LiCl-3. (f) TEM of CHM@LiCl-3, and the corresponding element mapping images of Cr, O, C, Cl. (g) XRD patterns, (h) FTIR spectra and (i) XPS spectra of MIL-101(Cr), HM, CHM and CHM@LiCl-3.

pattern of CHM (Fig. 2g) shows a broad peak, relating to the porous carbon structure. And it also indicates that the carbonization process disrupted the ordered crystalline structure of HM. However, the CHM retains most of the absorption peaks in FTIR spectrum (Fig. 2h) of HM, with the changes around 1600 cm^{-1} likely resulting from partial pyrolysis of the organic ligands during carbonization.

After impregnation with LiCl, the characteristic peaks (Fig. 2g and S1b) of CHM@LiCl were corresponded to LiCl (PDF#74-1181) and LiCl H$_2$O (PDF#22-1142), and the intensity was gradually enhanced with the increasing LiCl loading from 6.3 to 13.4 wt%. Specifically, the peak at 32.8° corresponds to the (202) crystal plane of LiCl H$_2$O, while the peaks at 30.09° and 34.88° are attributed to the (111) and (200) crystal planes of LiCl, respectively. These results confirm the successful loading of LiCl into CHM. Furthermore, as can be seen from the SEM images (Fig. 2e and S3), with the increase in LiCl loading, the shape of the porous carbon spheres becomes increasingly close to spherical, and the surface wrinkles gradually disappear. However, from several carbon spheres with holes, the intactness of their internal cavity structure can be observed (Fig. 2e) after the loading of LiCl, indicating that the modification of LiCl does not alter the structure or morphology of CHM. This is further supported by the TEM images (Fig. 2f). It reveals that the hollow structure of the HM is preserved after carbonization. And the distribution of Cr, O, C, and Cl is uniform, which indicates that the porous carbon formed under appropriate pyrolysis conditions is conducive to the uniform loading of LiCl. Additionally, the peaks (Fig. 2h) between 747 and 1164 cm^{-1} are attributed to the C–H stretching vibrations. And the –OH stretching vibration is observed around 3400 cm^{-1}, confirming the hydrophilicity of the sample.

To better understand the chemical composition of the CHM@LiCl composite material, XPS full spectra and the C 1s, O 1s, and Cr 2p spectra were recorded, as shown in Fig. 2i and S5. In the XPS full spectrum, all the samples exhibit the peaks of C 1s, O 1s, and Cr 2p, and a Cl 2p after the loading of LiCl. Specifically, Fig. S5a shows the high-resolution C 1s spectrum, which features four sub-peaks at 284.8 eV, 288.6 eV, 286.0 eV, and 290.6 eV, corresponding to C–C/C=C, C=O, C–O, and π–π* electronic transition peaks, respectively.[30] The presence of C=O and C–O bonds can be attributed to the dicarboxylate linkers of MIL-101(Cr), which is consistent with the FTIR results in Fig. 2h. In the O 1s spectrum (Fig. S5b), peaks at 530 eV, 531.8 eV, and 533.6 eV correspond to Cr–O, C=O, and O–H bonds, respectively. The Cr 2p spectrum (Fig. S5c) consists of two peaks, Cr 2p$_{1/2}$ and Cr 2p$_{3/2}$. In MIL-101(Cr), these peaks appear at approximately 586.8 eV and 577.2 eV, corresponding to the typical binding energies of Cr in MIL-101(Cr).[31] After carbonization, a shift in the Cr 2p and O 1s peaks to lower binding energies is observed. The binding energies of Cr 2p$_{3/2}$ and Cr 2p$_{1/2}$ in Cr$_2$O$_3$ are 576.6 eV and 586.3 eV, respectively. The intensity of the C=O peak of CHM samples in the C 1s spectrum decreases, suggesting that partial decomposition of the organic ligands during carbonization, with a change of the coordination environment of Cr from the organic metal framework to the amorphous inorganic oxide (Cr$_2$O$_3$).[30] XRD,

FTIR, and XPS results all suggest that partial decomposition of organic ligands after carbonization, resulting in changes in the coordination environment of Cr and the formation of amorphous Cr$_2$O$_3$.

To investigate the effect of Cr on the structure of CHM, the CHM sample was immersed in an HCl solution (mixed 10 mL hydrochloric acid and 10 mL DI water) for 24 hours to remove Cr. The resulting sample was named as C. As shown in Fig. S6, the structure of CHM after the removal of Cr largely collapsed, with only a small amount of carbon sphere structure remaining. Additionally, the XPS full spectrum showed trace amounts of Cr, indicating that the removal of Cr leads to the collapse of the CHM framework. These results suggest that the amorphous chromium oxide is crucial for maintaining the hollow porous microstructure of CHM.

N$_2$ sorption isotherms and pore size distribution results of the samples are shown in Fig. 3a, b and Table S2. MIL-101, HM, and CHM samples exhibit typical IV isotherms, with a rapid increase in adsorption at low pressures and a pronounced hysteresis at relative pressures above 0.8, indicating the presence of both micropores and mesopores.[29] The BET surface areas of MIL-101 and HM are 2644 m^2 g^{-1} and 2802 m^2 g^{-1}, respectively, and the pore volume slightly increased from 1.58 cm^3 g^{-1} to 1.63 cm^3 g^{-1}, which is attributed to the hollow structure and defects introduced by etching process. After carbonization, both the BET surface area and pore volume of CHM decreased (327.49 m^2 g^{-1}, 0.33 cm^3 g^{-1}), which is due to partial decomposition of the structure and the formation of amorphous Cr$_2$O$_3$. However, CHM still maintains a hierarchical porous structure, which is beneficial for the loading of LiCl and provides sufficient mass transfer pathways.[21] The CHM@LiCl-3 sample displays a type III isotherm, with a clear hysteresis loop, indicating the presence of irregular mesoporous structures.[32] After modification with LiCl, the BET surface area and pore volume of CHM@LiCl-3 further decreased (44.16 m^2 g^{-1}, 0.14 cm^3 g^{-1}), suggesting that LiCl was confined within the pore structure of CHM. The pore size distribution reveals that the micropores of CHM@LiCl-3 are larger than 0.85 nm, exceeding the kinetic diameter of water molecules (0.27–0.32 nm).[33] The hierarchical porous structure of CHM@LiCl-3 is beneficial for the fast diffusion, transport and storage of water vapor.

To investigate the photothermal properties of the materials, the light absorption capacity and photothermal behavior of the HM and CHM@LiCl-3 samples were evaluated. The UV-vis-NIR spectrum reveals that CHM@LiCl-3 exhibits excellent broadband solar absorption (~90%) in the ultraviolet-visible range, as shown in Fig. 3c. Compared to HM, CHM@LiCl-3 demonstrates improved light absorption across the entire AM1.5G solar spectrum, which is beneficial for the solar-driven fast water release process. Superior light absorption capability is fundamental for efficient photothermal conversion. Fig. 3d presents the surface temperature change curves of dried CHM@LiCl-3 under different simulated solar irradiation intensities, which is monitored by an infrared camera. Under 1 kW m^{-2} (1 Sun) irradiation, the surface temperature of CHM@LiCl-3 rapidly increases from 29.4 °C to 58.9 °C within 2 minutes and continues rising, reaching 67 °C after 10 minutes. When the
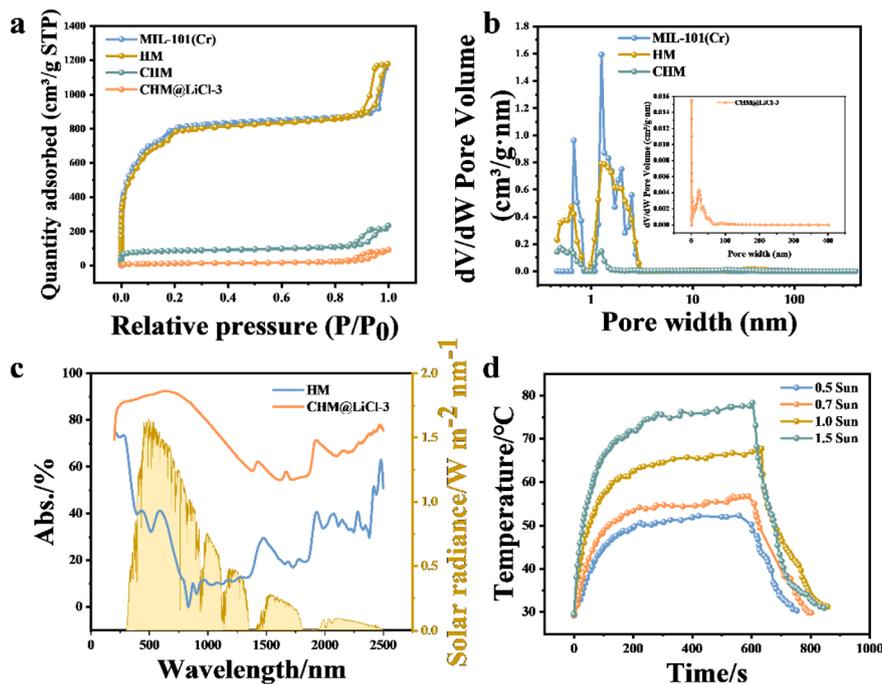
Fig. 3 (a) The N$_2$ adsorption–desorption isotherms of MIL-101(Cr), HM, CHM and CHM@LiCl-3. (b) Pore size distribution curves of MIL-101(Cr), HM, CHM and CHM@LiCl-3. (c) UV-vis-NIR absorption spectra of HM and CHM@LiCl-3. (d) Temperature change curves of CHM@LiCl-3 depend on time under different light intensities.

irradiation intensity is increased to 1.5 Sun, the surface temperature rises from ambient temperature (∼30 °C) to 78.4 °C within 10 minutes. Even under lower irradiation intensities of 0.7 Sun and 0.5 Sun, the surface temperature reaches 57.0 °C and 53.0 °C within 10 minutes, respectively, indicating its excellent sunlight utilization efficiency. After the removal of simulated sunlight, CHM@LiCl-3 undergoes a rapid cooling process, demonstrating its effective and reversible photothermal responsiveness.[34]

Water sorption–desorption performance and kinetics of CHM@LiCl

To evaluate the water adsorption capacity of the adsorbent samples across a wide range of humidity, the water adsorption isotherms of all samples were first tested at 25 °C. MIL-101(Cr) and HM adsorbents exhibit an "S-shaped" isotherm, with sharply changes in water uptake occurring in the range of 30–50% RH (see Fig. 4a). At 60% RH and 25 °C, the water adsorption capacity of MIL-101(Cr) reaches as high as 0.9 g g^{-1}. This is attributed to the porous structure and capillary condensation of MIL-101(Cr).[29] However, the pure MIL-101(Cr) is usually employed for SAWH in high RH regions, and it is not suitable for AWH in arid climates (30% RH).[35] By contrast, HM with hollow structure shows an increase in water adsorption capacity at 30% RH and keeps a higher water adsorption performance (from 0.068 g g^{-1} to 0.095 g g^{-1}), which indicates that the hollow cavities and hierarchical porous structure of HM significantly improve the water uptake capability at 30% RH. The water adsorption capacity is influenced by factors such as

the pore structure of sorbents, specific surface area, hydrophilic active sites, and defects.[35] The increased specific surface area and pore volume of HM samples, and the introduced of more structural defects, which not only reduce the resistance to water vapor diffusion in the pores but also enhance water adsorption capacity.[36] Nonetheless, both HM and MIL-101(Cr) still exhibit limited water adsorption capacity at RH below 30% and low light absorption ability, thus requiring additional photothermal components to facilitate the solar-driven desorption process.

The water adsorption capacity of CHM in the low-humidity range (10–40% RH) is comparable to that of MIL-101(Cr) (0.04–0.08 g g^{-1}). However, due to the hydrophobic nature of porous carbon, its maximum adsorption capacity remains at 0.20 g g^{-1}. After modification with LiCl, it is observed that as the LiCl content increases, the CHM@LiCl composite exhibit improved water adsorption capabilities across a wide range of humidity, as shown in Fig. 4a and S7a. Notably, the water adsorption performance of CHM@LiCl is higher than that of the HM precursor in both low- and high-humidity regions. At 20% RH, the adsorption capacities of CHM@LiCl-1, CHM@LiCl-2, and CHM@LiCl-3 are 2.11, 2.46, and 4.39 times as that of HM, respectively. At 40% RH, CHM@LiCl-3 shows an adsorption capacity comparable to that of HM (0.39 g g^{-1}) and is five times greater than that of MIL-101(Cr). The maximum adsorption capacity of CHM@LiCl-3 can reach 2.07 g g^{-1}, nearly double that of the MIL-101(Cr). The high water uptake of CHM@LiCl adsorbents is mainly attributed to the chemical adsorption of LiCl.[12] The water adsorption capacity of CHM@LiCl-3 is higher than that of CHM@LiCl-1 (1.11 g g^{-1}) and CHM@LiCl-2 (1.31 g g^{-1}), primarily because the higher LiCl
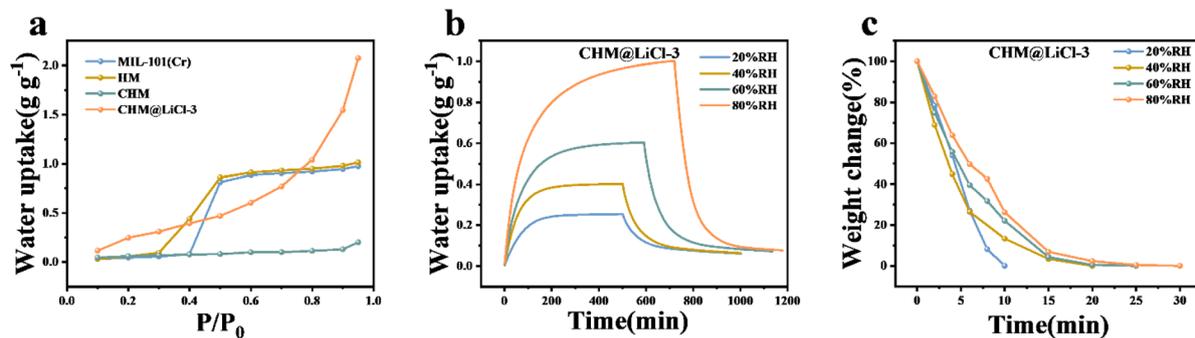
Fig. 4 (a) Water vapor sorption isotherms of MIL-101(Cr), HM, CHM and CHM@LiCl-3. (b) The static water sorption curves at 20%, 40%, 60% and 80% RH for CHM@LiCl-3. (c) Weight change curves of sorbents under simulated sunlight for CHM@LiCl-3.

loading in CHM@LiCl-3 provides more adsorption sites for water. However, a higher salt load will bring the risk of salt leakage and occupy more pore volume, hindering the adsorption kinetics. Compared to CHM, LiCl in CHM@LiCl-3 has already occupied 58% of the pore volume (Table S2). Additionally, the water adsorption tests of C sample with the removal of Cr reveal that its maximum adsorption capacity is below 0.12 g g^{-1} (Fig. S7b), far lower than that of CHM (0.20 g g^{-1}). This indicates that the pore structure of the carbon material is collapsed after the removal of chromium oxides, which also supported by its BET surface area (20.21 m^2 g^{-1}) much lower than that of CHM (327.49 m^2 g^{-1}).

Fast adsorption–desorption kinetics is one of the essential characteristics of ideal solar-driven SAWH materials. Static water adsorption, and solar-driven water release tests were conducted on different samples under constant temperature and humidity conditions. The static water adsorption curves of various adsorbents at 25 °C and 20–80% RH are shown in Fig. 4b and S8. The saturated adsorption capacity of each adsorbent increases with the increment of humidity. The adsorption kinetics of HM and MIL-101(Cr) are significantly affected by humidity, with longer time (4–13 hours) required to reach equilibrium in the moderate humidity range (Fig. S8a and b). In contrast, CHM with hierarchical pore structure and hydrophobicity exhibits fast adsorption kinetics, and can achieve saturation in almost 60 minutes. After loading with LiCl, the adsorption capacity of CHM@LiCl composite adsorbents increases significantly, and the adsorption kinetics of CHM@LiCl composites slightly decline as the LiCl content increases. All CHM@LiCl adsorbents with different LiCl loadings show rapid water uptake within the first 100 minutes (Fig. 4b, S8d and e), with nearly 90% of the total capacity adsorbed within 200 minutes. Compared to CHM, the adsorption capacity of CHM@LiCl-3 increases by 4.2, 5.3, 6.1, and 9.1 times at 20%, 40%, 60% and 80% RH, respectively. The enhancement of capacity is primarily due to the hollow porous structure of CHM, providing ample pore space for the loading and even distribution of LiCl. LiCl as the main adsorption site in the composite adsorbent, can fully interact with water vapor through the porous structure. Additionally, the cavities in CHM

provide space for storage of the adsorbed water, ultimately improving the overall adsorption capacity of CHM@LiCl-3.

A macro-scale linear driving model was used to calculate the equilibrium adsorption capacity w_e (g g^{-1}) and the adsorption rate constant k for different adsorbents. The results are shown in Tables S3 and S4. A higher k value indicates a faster adsorption rate, meaning the adsorbent reaches saturation in a shorter time. As shown in Tables S3 and S4, the equilibrium adsorption capacity w_e increases with the content of salt, while the adsorption rate constant k decreases. This is because the hygroscopic salt LiCl, as adsorption sites, significantly enhance the affinity for water vapor, thereby improving the equilibrium adsorption capacity. The adsorption kinetics of the CHM matrix are faster than those of the CHM@LiCl adsorbents, as evidenced by the static adsorption curves. This difference arises from the inherently low adsorption rate of LiCl and the worse capacity of CHM. Since mesopores facilitate the diffusion and transport of water molecules, the pore volume of the CHM@LiCl sorbent decreases upon the incorporation of LiCl, which leads to an increase in diffusion resistance. This reduction in pore volume can hinder the efficient movement of water molecules within the material, thereby resulting in longer adsorption equilibrium times and a lower adsorption rate constant, when compared to the CHM sorbents without LiCl. This trend is consistent with previous reports.[37,38]

As the relative humidity increases from 20% RH to 80% RH, the equilibrium adsorption capacity w_e of each adsorbent increase, and the adsorption rate constant k generally decreases. During the water adsorption process, LiCl undergoes three stages: the formation of hydrates, deliquescence, and the absorption of salt solution. As the RH increases, LiCl forms a solution during the adsorption process, causing the adsorption mechanism to shift from solid–gas adsorption to liquid–gas absorption. The dissolution of LiCl in the adsorbed water leads to a reduction in the effective contact area between LiCl and water molecules, which in turn inhibits the diffusion of water molecules within the sorbent. As LiCl interacts with the adsorbed water, it forms a more stable hydrated phase, thereby limiting the mobility of water molecules. This reduced contact area between the salt and the water molecules hinders the efficient diffusion of water through the porous structure,

slowing down the overall water uptake capacity. Besides, the dissolved LiCl can create localized areas with higher ionic concentrations, which may affect the kinetic of sorbents.[39]

In addition to water adsorption capacity, desorption characteristics also determine the ultimate water collection performance. The solar-driven water release performance of the hollow porous carbon and its composites were investigated under simulated sunlight (1 kW m^{-2}) using a xenon lamp. The weight change curves of the adsorbents are shown in Fig. 4c and S9. Due to the excellent photothermal properties of the MOFs-derived hollow-structured porous carbon spheres, efficient photothermal conversion is achieved. When the adsorbent is exposed to simulated sunlight, photothermal effects induce an increase in the temperature of the adsorbent, leading to the fast release of water. The CHM adsorbent can release nearly 100% of the water within 10 minutes. By contrast, the CHM@LiCl composite rapidly releases ~80% of the water in the first 10 minutes and releases all the adsorbed water within 30 minutes, demonstrating its excellent photothermal water desorption performance. In traditional solar-driven water release processes, the photothermal components and the adsorbent are separate, with heat generated at the top photothermal layer and subsequently transferred to the adsorbent. This process causes abundant heat loss, leading to lower solar energy utilization efficiency.[40] In contrast, in CHM@LiCl adsorbents, heat is generated by the structure of hollow porous carbon, which presents great thermal conductivity, allowing heat to be evenly distributed within the carbon matrix, and then in turn heating the LiCl sites from multiple directions to release water. The heat loss was reduced, resulting in superior rapid photothermal dehydration performance. Compared to the higher energy barrier of pure LiCl during the dehydration process,[15] the CHM@LiCl composite demonstrates a distinct advantage in the solar-driven water release process, enabling efficient dehydration without the need for external energy input.

Water sorption–desorption performance and kinetics of LiCl in the CHM@LiCl

To evaluate the contribution of LiCl in the CHM@LiCl composite adsorbent, the water adsorption capacity of LiCl in CHM@LiCl was calculated to better compare its performance. According to the thermodynamic model, the water adsorption capacity of pure LiCl at 25 °C under different humidity conditions is reported as 1.49 g g^{-1} (20% RH), 2.24 g g^{-1} (40% RH), 3.23 g g^{-1} (60% RH), and 5.52 g g^{-1} (80% RH).[12] The static adsorption performance of LiCl in the CHM@LiCl composite were calculated according to Fig. 4b and S8, and the results are shown in Fig. S10. The maximum water adsorption capacities of LiCl in CHM@LiCl-3 at 20% RH, 40% RH, 60% RH, and 80% RH are 1.51 g g^{-1}, 2.52 g g^{-1}, 3.86 g g^{-1}, and 6.75 g g^{-1}, respectively (Fig. S10d). These values are better than those of pure LiCl, which can be explained as follows: during the water adsorption process, pure LiCl capture water vapor to form droplets, which then coalesce into larger droplets. This aggregation results in a reduction of the surface area available for exposure to air, which subsequently impedes the diffusion of

water vapor into the sorbent material. In contrast, CHM possesses a hollow and hierarchical porous structure, which provides ample loading sites for LiCl, allowing it to be evenly dispersed throughout the CHM matrix. This increases the contact area between LiCl and water molecules, enhancing the effectivity of active sites, and thus results in higher adsorption capacity of CHM@LiCl composite at low to high humidity.

Pure LiCl exhibits a slow adsorption rate and is difficult to reach saturation within a short period.[41] In contrast, the LiCl in the CHM@LiCl composite can adsorb nearly 90% of its total capacity within 200 minutes. Previous literature reports that pure LiCl only reaches an adsorption capacity of 1.64 g g^{-1} (60% RH) and 2.65 g g^{-1} (80% RH) within 7 hours.[42] The comparison of water uptake performance is shown in Table S5. Although the loading amount of lithium chloride in this work is relatively low, the actual water absorption capacity is better than most of those reported in the literature.[15,18,42–49] Moreover, the low loading amount also helps to prevent salt leakage and improve the long-term utilization. Clearly, LiCl in the CHM@LiCl composite adsorbent exhibits faster adsorption kinetics. This is attributed to the larger specific surface area and pore volume of CHM@LiCl compared to pure LiCl, which facilitates the contact between the sorbents and water vapor in the air, thereby promoting the water adsorption kinetics of LiCl in the composite adsorbent.

Water harvesting performance of CHM@LiCl-3

The solar-driven SAWH performance of the CHM@LiCl-3 in real environmental conditions was tested to demonstrate its feasibility. The water harvester is a custom-designed transparent cubic container. Initially, the pre-dried CHM@LiCl-3 was placed in the open container to fully adsorb water from the environment (June 23, 2024, Wenzhou, China, 23.5 °C, and the relative humidity ranged between 60% RH and 65% RH). Based on the adsorption kinetics of CHM@LiCl-3, after 200 minutes of adsorption, the adsorbent was sealed inside the water collector. The subsequent desorption process was carried out under simulated sunlight using a xenon lamp with an irradiance of 1 kW m^{-2}. Throughout the water adsorption and solar-driven desorption process, the optical images of the water collector, along with the corresponding changes in environmental temperature and humidity, are shown in Fig. 5a and b. Fig. 5a illustrates the water released and condensed on the inner wall of the water collector after the desorption process. The CHM@LiCl-3 adsorbent could complete one water collection cycle within 230 minutes, with the water adsorption, release, and collection capacities of 0.60 g g^{-1}, 0.596 g g^{-1}, and 0.53 g g^{-1}, respectively. Under these conditions, the water collection efficiency (η) of CHM@LiCl-3 was 89.1%.

In addition, the cycling stability of the CHM@LiCl-3 adsorbent was tested. The conditions were set as follows: adsorption was performed at 25 °C and 60% RH, and desorption was carried out under 1 Sun. The adsorption–desorption process was repeated for 10 times. As shown in Fig. 5c, the water adsorption capacity during the first cycle was 0.60 g g^{-1}, with nearly complete release of the adsorbed water. After ten times of
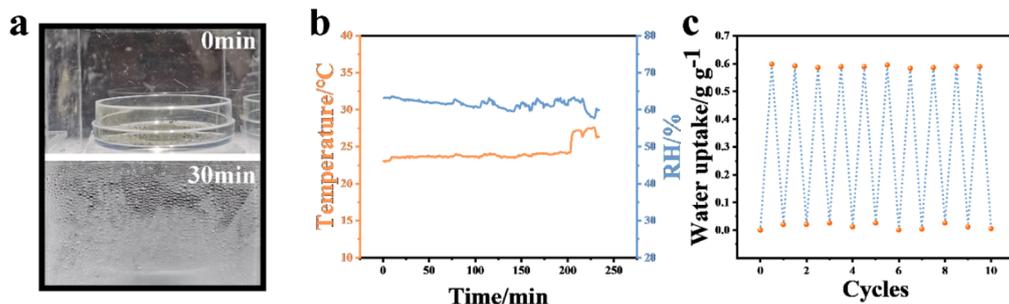
Fig. 5 (a) Optical images of the water harvester during the water release process. (b) The ambient temperature and humidity change curves during the water harvesting process. (c) The water sorption–desorption cycling tests of CHM@LiCl-3 at 25 °C, 60% RH for sorption and then exposed to simulated sunlight at 1 kW m^{-2} for desorption.

the adsorption–desorption cycles, the performance of CHM@LiCl-3 exhibited slight fluctuations with no significant degradation. This indicates that CHM@LiCl-3 presents excellent operational stability and can maintain a considerable water adsorption–desorption capacity over multiple cycles, demonstrating its potential to achieve higher water yield through repeated cycles.

Conclusions

In this study, we prepared a unique MOFs-derived porous carbon hollow microspheres modified by hygroscopic LiCl salt for SAWH. The hollow-structured MIL-101(Cr) spheres were obtained by an etching method and carbonized to porous carbon hollow microspheres (CHM). Then LiCl was impregnated into CHM to form CHM@LiCl sorbent. The hydrophilic LiCl significantly enhances the overall water adsorption capacity. The hierarchical porous CHM provides high porosity and excellent photothermal ability, enabling rapid water adsorption and fast solar-driven water release. The adsorbed water can be released under sunlight within 30 minutes. Besides, the hollow porous structure is beneficial for the uniform dispersion of LiCl within the CHM, thus achieving superior water adsorption performance than that of the pure LiCl, and effectively mitigates the issue of salt leakage. The rapid kinetics of CHM@LiCl-3 enable it to collect 0.53 liters of water per kilogram of adsorbent within 230 minutes under realistic conditions. Moreover, after multiple cycles, it maintains excellent adsorption capacity and 100% dehydration rate. This may provide a new way for designing MOFs-derived porous carbon adsorbents for solar-driven SAWH.

Experimental

Chemicals and materials

Chromium nitrate hydrate (Cr(NO$_3$)$_3$·9H$_2$O, 99%), 1,4-benzene dicarboxylate (C$_8$H$_6$O$_4$, 1,4-BDC, 99%) and lithium chloride (LiCl, 99%) were purchased from Aladdin. N,N'-dimethyl formamide (C$_3$H$_7$NO, DMF, AR) was obtained from Macklin. Acetic acid (CH$_3$COOH, AR), hydrochloric acid (HCl, AR) and ethanol (C$_2$H$_5$OH, AR) were purchased from Sinopharm Chemical Reagent Co., Ltd. Deionized (DI) water (18.2 MΩ cm, from Milli-

Q system) was used in all experiments. All the chemicals were used without further purification.

Synthesis of MIL-101(Cr)

MIL-101(Cr) was synthesized according to the reported hydrothermal method.[50] Cr(NO$_3$)$_3$·9H$_2$O (5 mmol, 2 g) and 1,4-BDC (5 mmol, 0.83 g) were dissolving in DI water (25 mL) under ultrasonication for 30 minutes. The mixture was then transferred to a 50 mL Teflon-lined container, sealed and placed in a hydrothermal reactor. Subsequently, the reactor was placed in a preheated oven at 220 °C for 8 hours. After cooling to room temperature, the green solid product was obtained by centrifugation (10000 rpm) for 10 minutes. The precipitate was washed three times with hot DMF and ethanol respectively, centrifugated and dried at 120 °C for 12 hours. Finally, green MIL-101(Cr) was obtained.

Synthesis of the HM

Hollow MIL-101(Cr) (HM) was prepared by acetic acid etching.[28] Cr(NO$_3$)$_3$·9H$_2$O (2 mmol, 0.8 g), 1,4-BDC (1.32 mmol, 0.22 g) and DI water (20 mL) were mixed and treated in the ultrasonic machine for 10 minutes. The obtained uniform dispersion was then transferred to the Teflon-lined container, and then heated at 180 °C for 4 hours in the oven. When cooling to room temperature, the precipitate was obtained by centrifugation (10000 rpm) for 10 minutes and washed three times with DMF and DI water respectively, followed by re-dispersion in DI water (20 mL). The dispersion was mixed with acetic acid (2 mL) and DI water (20 mL), placed in the Teflon-lined container and heated at 180 °C for 4 hours. After cooling to room temperature, the dark green HM was obtained by centrifugation (10000 rpm) for 10 minutes, washed three times with DMF and DI water respectively. Then the HM was activation by methanol solvent exchange and dried at 120 °C for 12 hours.

Synthesis of the CHM

The HM was converted into CHM through high-temperature carbonization. The carbonization conditions were as follows: a certain amount of HM was placed in a ceramic crucible positioned at the center of a tube furnace with an argon atmosphere, the temperature was raised from room temperature to

400 °C at a rate of 10 °C min^{-1} and maintained at 400 °C for 3 hours. After cooling to room temperature, the porous carbon material (CHM) was obtained.

Synthesis of the CHM@LiCl sorbents

The CHM@LiCl composite material was obtained *via* an impregnation method. Specifically, CHM was immersed in aqueous LiCl solutions of varying concentrations (0.02 g mL^{-1}, 0.04 g mL^{-1}, and 0.06 g mL^{-1}). Subsequently, the products were collected using a vacuum filtration system and dried at 120 °C for 8 hours. The resulting CHM@LiCl composites, with different LiCl contents, were named as CHM@LiCl-1, CHM@LiCl-2, and CHM@LiCl-3, respectively (Table S1).

Characterization

The powder XRD data were collected on X-ray powder diffractometers (SmartLab, 5–50°, Cu Kα). SEM images were acquired using a Sigma 300. The XPS data were acquired with AXIS SUPRA, Kratas. The FTIR spectra were recorded on a Nicolet Is5 (Thermo Fisher) with KBr pellets as background in the range 4000–400 cm^{-1}. UV-vis-NIR spectra were measured by a spectrometer (UV-3600) with an integrating sphere in the wavelength range of 2500 to 200 nm. N$_2$ sorption isotherms were recorded on an American Mike ASAP 2460 instrument. A Xenon lamp (CELPE300-3A) with a standard AM1.5G optical filter was used to simulate sunlight, and the optical intensity was measured with an optical power density meter (CEL-NP2000). Infrared camera (FLIR, E40) was used to record the photothermal data. Volumetric water adsorption isotherms are obtained on a BELSORP-MAXII instrument. Temperature and humidity were recorded on a data logger (COS-03) automatically.

Water sorption and desorption experiment

The water vapor adsorption isotherms were measured using a Beishide Dynamic Vapor/Gas Sorption Analyzer (BSD-DVS). All the samples (30 mg) were degassed under vacuum at 120 °C for 4 hours before test. During the test, the temperature was set at 25 °C and the humidity was gradually increased by adjusting the ratio of N$_2$ and water vapor.

Static water adsorption tests were also conducted by the BSD-DVS instrument under the following conditions: constant temperature of 25 °C and relative humidity settings of 20% RH, 40% RH, 60% RH, and 80% RH. All the samples (30 mg) were degassed under vacuum at 120 °C for 4 hours before test.

Solar-driven water desorption: firstly, all the samples (30 mg) were activated overnight at 120 °C, and then placed in a pre-set constant temperature and humidity chamber for sorption saturation (temperature: 25 °C, relative humidity settings of 20% RH, 40% RH, 60% RH, and 80% RH). After completing the adsorption process, the samples were exposed to the simulated sunlight with 1 kW m^{-2} (1 Sun), and the ambient humidity maintained at ~55% RH. The weight change of the samples was monitored throughout the process using an analytical balance.

Author contributions

Jiake Jin: primary investigation, formal analysis, and original draft writing and editing. Simiao Guo: primary investigation, methodology. Yue Hu: data analysis, reviewing and editing. Yefeng Yang: data analysis, reviewing and editing, funding acquisition. Pingwei Ye: conceptualization, reviewing and editing, resources. Xinsheng Peng: conceptualization, supervision, reviewing and editing, resources.

Conflicts of interest

There are no conflicts to declare.

Data availability

The data supporting this article have been included as part of the supplementary information (SI). Supplementary information: the detail equations for the calculations, additional XRD patterns, FTIR spectra, SEM images, XPS spectra, water vapor sorption isotherms, the static water sorption curves, weight change curves of sorbents under simulated sunlight, histogram of size statistics of the samples and additional Tables S1 to S4. See DOI: https://doi.org/10.1039/d5ra04196a.

Acknowledgements

References

1 M. M. Mekonnen and A. Y. Hoekstra, *Sci. Adv.*, 2016, **2**, e1500323.

2 E. R. Jones, M. F. P. Bierkens and M. T. H. van Vliet, *Nat. Clim. Change*, 2024, **14**, 629–635.

3 S. H. Schneider, T. L. Root and M. D. Mastrandrea, *Encyclopedia of Climate and Weather*, Oxford University Press, 2011.

4 A. K. Misra, G. Agrawal and A. Yadav, *Int. J. Numer. Method. H.*, 2025, **35**(8), 2697–2724.

5 M. J. Zeng, Z. G. Qu and J. F. Zhang, *Sep. Purif. Technol.*, 2023, **305**, 122465.

6 D. Yang, A. G. Ramu, M. Song and D. Choi, *Chem.–Eng. J.*, 2025, **505**, 159001.

7 Z. Bai, P. Wang, J. Xu, R. Wang and T. Li, *Sci. Bull.*, 2024, **69**, 671–687.

8 S. Nishad, H. M. Elmoughni and I. Krupa, *Appl. Energy*, 2025, **377**, 124576.

9 W. Xu and O. M. Yaghi, *ACS Cent. Sci.*, 2020, **6**, 1348–1354.

10 F. Fathieh, M. J. Kalmutzki, E. A. Kapustin, P. J. Waller, J. Yang and O. M. Yaghi, *Sci. Adv.*, 2018, **4**, eaat3198.

11 M. Cheng, X. Lian, H. Bai, X. Wang, J. Xu, M. Cao and X. H. Bu, *Adv. Funct. Mater.*, 2024, **35**, 2416241.

12 H. Shan, P. Poredoš, Z. Chen, X. Yang, Z. Ye, Z. Hu, R. Wang and S. C. Tan, *Nat. Rev. Mater.*, 2024, **9**, 699–721.

13 H. Zhang, Z. Zhou, J. Du, X. Pei and L. Zhou, *J. Clean. Prod.*, 2023, **416**, 137897.

14 J. Wang, W. Ying, B. Lin, C. Li, C. Deng, H. Zhang, S. Wang and R. Wang, *Adv. Mater.*, 2024, **36**, 2408977.

15 T. Li, T. Yan, P. Wang, J. Xu, X. Huo, Z. Bai, W. Shi, G. Yu and R. Wang, *Nat. Water*, 2023, **1**, 971–981.

16 W. Guan, Y. Zhao, C. Lei, Y. Wang, K. Wu and G. Yu, *Adv. Mater.*, 2025, **37**, 2420319.

17 J. Sun, F. Ni, J. Gu, M. Si, D. Liu, C. Zhang, X. Shui, P. Xiao and T. Chen, *Adv. Mater.*, 2024, **36**, 2314175.

18 X. Xu, W. Liu, T. Xian, F. Foroughi, S. Zhou and J. Ding, *Adv. Funct. Mater.*, 2024, **34**, 2402671.

19 Y. Hu, Z. Fang, B. Yao, Z. Ye and X. Peng, *Appl. Mater. Today*, 2024, **37**, 102121.

20 Y. Ying, G. Yang, Y. Tao, Q. Wu and H. Li, *Adv. Sci.*, 2023, **10**, 2204840.

21 J. Xu, T. Li, J. Chao, S. Wu, T. Yan, W. Li, B. Cao and R. Wang, *Angew. Chem., Int. Ed.*, 2020, **59**, 5202–5210.

22 Z. Li, X. Xu, X. Sheng, P. Lin, J. Tang, L. Pan, Y. V. Kaneti, T. Yang and Y. Yamauchi, *ACS Nano*, 2021, **15**, 12535–12566.

23 Y. Hu, Z. Fang, X. Ma, X. Wan, S. Wang, S. Fan, Z. Ye and X. Peng, *Appl. Mater. Today*, 2021, **23**, 101076.

24 H. Guo, Q. Luo, D. Liu, X. Li, C. Zhang, X. He, C. Miao, X. Zhang and X. Qin, *Adv. Mater.*, 2024, **36**, 2414285.

25 G. Férey, C. Mellot-Draznieks, C. Serre, F. Millange, J. Dutour, S. Surblé and I. Margiolaki, *Science*, 2005, **309**, 2040–2042.

26 W. Liu, J. Huang, Q. Yang, S. Wang, X. Sun, W. Zhang, J. Liu and F. Huo, *Angew. Chem., Int. Ed.*, 2017, **56**, 5512–5516.

27 Y. Xia, Y. Xiong, B. Lim and S. E. Skrabalak, *Angew. Chem.*, 2009, **121**, 62–108.

28 U. Adamu, N. H. H. Abu Bakar, Z. U. Zango, N. S. Sambudi, A. Iqbal, M. H. Hussin and T. S. Hamidon, *Korean J. Chem. Eng.*, 2023, **40**, 2239–2252.

29 X. Yang, H. Zhang, J. Gao, Y. Yao, Y. Zhou, J. Qi, Y. Yang, Z. Zhu and J. Li, *Adv. Fiber Mater.*, 2024, **6**, 1969–1979.

30 Y. Hu, Z. Fang, X. Wan, X. Ma, S. Wang, S. Fan, M. Dong, Z. Ye and X. Peng, *Chem.–Eng. J.*, 2022, **430**, 133086.

31 A. Farisabadi, M. Moradi, S. Hajati, M. A. Kiani and J. P. Espinos, *Appl. Surf. Sci.*, 2019, **469**, 192–203.

32 P. Hou, G. Xing, D. Han, Y. Zhao, G. Zhang, H. Wang, C. Zhao and C. Yu, *J. Porous Mater.*, 2019, **26**, 1607–1618.

33 X. Chen, X. Chen, S. Cai, J. Chen, W. Xu, H. Jia and J. Chen, *Chem. Eng. J.*, 2018, **334**, 768–779.

34 A. Li, J. Xiong, Y. Liu, L. Wang, X. Qin and J. Yu, *Energy Environ. Mater.*, 2022, **6**, e12254.

35 S. Dang, Q.-L. Zhu and Q. Xu, *Nat. Rev. Mater.*, 2017, **3**, 17075.

36 N. Hanikel, M. S. Prévot and O. M. Yaghi, *Nat. Nanotechnol.*, 2020, **15**, 348–355.

37 X. Liu, X. Wang and F. Kapteijn, *Chem. Rev.*, 2020, **120**, 8303–8377.

38 B. Dawoud and Y. I. Aristov, *Int. J. Heat Mass Tran.*, 2003, **46**, 273–281.

39 Y. Sun, A. Spieß, C. Jansen, A. Nuhnen, S. Gökpinar, R. Wiedey, S.-J. Ernst and C. Janiak, *J. Mater. Chem. A*, 2020, **8**, 13364–13375.

40 Y. Hou, Z. Sheng, C. Fu, J. Kong and X. Zhang, *Nat. Commun.*, 2022, **13**, 1227.

41 R. Li, Y. Shi, M. Wu, S. Hong and P. Wang, *Nano Energy*, 2020, **67**, 104255.

42 W. Guan, C. Lei, Y. Guo, W. Shi and G. Yu, *Adv. Mater.*, 2024, **36**, 2207786.

43 X. Han, L. Zhong, L. Zhang, L. Zhu, M. Zhou, S. Wang, D. Yu, H. Chen, Y. Hou and Y. Zheng, *Small*, 2023, **19**, 2303358.

44 J. Chen, M. Zhu, G. He, H. Yang, Z. Deng, J. Du, X. Liu, J. Huang, S. Gu and B. Shang, *Desalination*, 2025, **595**, 118319.

45 H. Lu, W. Shi, J. H. Zhang, A. C. Chen, W. Guan, C. Lei, J. R. Greer, S. V. Boriskina and G. Yu, *Adv. Mater.*, 2022, **34**, 2205344.

46 K. Lu, C. Liu, J. Liu, Y. He, X. Tian, Z. Liu, Y. Cao, Y. Shen, W. Huang and K. Zhang, *ACS Appl. Mater. Int.*, 2022, **14**, 33032–33040.

47 J. Wang, W. Ying, B. Lin, C. Li, C. Deng, H. Zhang, S. Wang and R. Wang, *Adv. Mater.*, 2025, **37**, 2408977.

48 T. Li Xu, J. Chao, S. Wu, T. Yan, W. Li, B. Cao and R. Wang, *Angew. Chem., Int. Ed.*, 2020, **59**, 5202–5210.

49 J. Xu, T. Li, T. Yan, S. Wu, M. Wu, J. Chao, X. Huo, P. Wang and R. Wang, *Energy Environ. Sci.*, 2021, **14**, 5979–5994.

50 P. Zhu, Z. Yu, H. Sun, D. Zheng, Y. Zheng, Y. Qian, Y. Wei, J. Lee, S. Srebnik, W. Chen, G. Chen and F. Jiang, *Adv. Mater.*, 2024, **36**, 2306653.